High precision detection of change in intermediate range order of amorphous zirconia-doped tantala thin films due to annealing

Kiran Prasai,[1,*] Jun Jiang,[2] Alec Mishkin,[2] Svetoslava Angelova,[3] Ross Birney,[3] David A Drabold,[4] Mariana Fazio,[5] Eric Gustafson,[6] Gregory Harry,[7] Sarah Hoback,[7] Carl Lévesque,[8] Ian MacLaren,[9] Iain W Martin,[9] Carmen S Menoni,[5] Steven Penn,[10] Stuart Reid,[3] Raymond Robie,[9] François Schiettekatte,[8] Rosalie Shink,[8] Badri Shyam,[11] Gabriele Vajente,[6] Hai-Ping Cheng,[2] Martin M Fejer,[1] Apurva Mehta,[12] and Riccardo Bassiri[1,†]

[1]*E. L. Ginzton Laboratory, Stanford University, Stanford, California 94305, USA*
[2]*Department of Physics and Quantum Theory Project, University of Florida, Gainesville, Florida 32611, USA*
[3]*SUPA, Department of Biomedical Engineering, University of Strathclyde, Glasgow G1 1QE, United Kingdom*
[4]*Department of Physics and Astronomy, Ohio University, Athens, Ohio 45701, USA*
[5]*Department of Electrical and Computer Engineering, Colorado State University, Fort Collins, Colorado 80523, USA*
[6]*LIGO Laboratory, California Institute of Technology, Pasadena, California 91125, USA*
[7]*Department of Physics, American University, Washington, DC 20016, USA*
[8]*Department of Physics, Université de Montréal, Québec H3T 1J4, Canada*
[9]*SUPA, School of Physics and Astronomy, University of Glasgow, Glasgow G12 8QQ, UK*
[10]*Department of Physics, Hobart and William Smith Colleges, Geneva, New York 14456, USA*
[11]*University of Dayton Research Institute, Dayton, Ohio 45469, USA*
[12]*SLAC National Accelerator Laboratory, Menlo Park, California 94025, USA*

(Dated: January 18, 2019)

Intermediate range order (IRO) of amorphous thin films is difficult to measure and unambiguously interpret. Through x-ray scattering measurements on thin films of amorphous zirconia-doped-tantala (ZrO_2-Ta_2O_5), we present high precision detection of the change in the IRO as a function of post-deposition heat treatment (annealing). We present an integrated atomic modeling approach and show for the first time that the annealing-induced changes seen in measured pair distribution function (PDF) can be captured in atomic models with high accuracy. Structural analysis shows that the material has building blocks of metal-centred polyhedra and the effect of annealing is to alter the way the polyhedra connect with each other. We explain the observed changes in IRO in terms of a shift in the ratio of corner-sharing to edge-sharing polyhedra as a function of annealing. We compute the degree of orientational order in metal-metal correlations and speculate on the correlations between the observed changes in the IRO and measured mechanical loss of thin films.

A scientific and technological grand challenge lies in the ability to understand the atomic structure properties that govern the performance of functional amorphous materials, and enabling the accelerated discovery and development of improved materials. Amorphous thin film coatings, in particular, are technologically important materials that often limit the performance of a variety of precision measurements. For example, Brownian thermal noise, due to mechanical loss, is a significant impairment in thin film coatings used in atomic clocks [1] and interferometric gravitational-wave detectors [2], such as the Laser Interferometer Gravitational-wave Observatory (LIGO), Virgo and KAGRA. The research presented here is driven by the critical importance in developing thin-film coatings with lower mechanical losses, and hence lower Brownian thermal noise, to the performance of future generations of interferometric gravitational-wave detectors [3].

In general, the atomic structure of amorphous materials can be described in terms of short- and intermediate-range order (SRO and IRO, respectively); the long-range order (LRO), characteristic of crystals, is unambiguously absent [4, 5]. SRO generally describes the structural order up to the first coordination sphere measured as the first peak in the pair distribution function (PDF), which often resembles the amorphous material's crystalline counterpart. Despite the general agreement on the concept, the definition of distance boundaries in SRO can vary in the literature [6]. In this letter, we study zirconia-doped tantala and use the SRO to describe the order up to ~ 2.9 Å, which is where the first coordination polyhedra of the material end. The IRO describes the structural organization that is *intermediate* between the discrete chemical bonds described in the SRO and the periodic lattice described in the LRO, and is the highest level of structural organization in amorphous materials. However, the IRO is less well understood than the SRO, and is more dependent on the details of how the material was synthesized or deposited.

Post-deposition annealing of amorphous thin films has been shown induce changes in both the atomic structure and mechanical loss [7, 8]. The structural changes associated with post-deposition annealing are often observed beyond the first coordination sphere, and lie in the IRO [9]. Even with tools that are best suited to probe the IRO, such as fluctuation electron microscopy (FEM) and

x-ray or neutron PDFs, the observed structural changes can be small and difficult to interpret. Accurate atomic modeling is required to capture the small changes in the atomic structure, and probe the IRO in detail.

In this paper, we demonstrate high precision atomic structure measurements and modeling of amorphous zirconia-doped tantala thin films that show small, but systematic, changes in IRO as a function of post-deposition annealing. We use grazing-incidence PDF (GIPDF) measurements and unprecedentedly sensitive atomic structure modeling that captures the local order changes accurately up to 15 Å. Finally, we discuss the implications of this increased understanding of the atomic structure and its relation to our efforts to reduce mechanical loss.

GIPDF data was collected from thin films of zirconia-doped tantala deposited by MLD Technologies (Mountain View, CA), were deposited by ion-beam sputtering with a Zr/(Zr+Ta) $\simeq$ 0.48, $\sim$ 590 nm in thickness (see [10]) on fused silica substrates. The target materials were pure metals in a partially pressurized oxygen environment, and the ambient temperature during deposition was less than 100°C. Post-deposition annealing of three different samples was carried out at 300, 600 and 800°C in air for 12 hours. GIPDF data was collected at the dedicated X-ray scattering beamline 10-2 at the Stanford Synchrotron Radiation Lightsource (SSRL), with q-range of 21 Å^{-1}. This unique GIPDF capability allows us to overcome a significant difficulty in measuring PDFs from thin films: a grazing incidence angle can be chosen that will enable the collection of X-rays scattered from the coatings and not the substrate. In addition, there is no destructive sample preparation, ensuring that the observed changes in the measured atomic structure do not result from the sample preparation process, which is especially relevant when looking at small structural changes due to annealing. Further details on the GIPDF data collection method are discussed in Refs [11–13]. The total scattering data was reduced to the normalized structure factor after applying corrections for air scattering, absorption, Compton scattering, polarization effects and geometric effects due to the detector footprint [13, 14].

The measured PDFs for one as-deposited and the three annealed samples are plotted in figure 1. At a first glance, all PDFs appear largely similar; all show a sharp first peak at 2.0(2) Å, a bifurcated second peak between 2.9(0) and 4.3(0) Å, and a series of smaller peaks between 5 Å and 15 Å. A closer look reveals a number of changes among the PDFs; the major changes, for example marked by letters a to f in figure 1, lie in the IRO. These include an increase in intensity of the peaks, appearance of new peaks, shifts in the position of the peaks and a deepening of the troughs. In most cases, the change is *systematic* with respect to the annealing temperature, an example is highlighted in the inset.

In order to better understand the annealing-induced

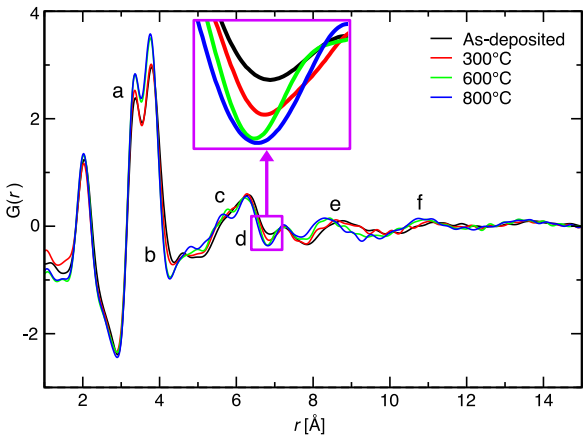

FIG. 1. **Detection of annealing induced changes:** Measured pair distribution functions (PDFs) of four thin films of zirconia-doped tantala are shown. The thin films differed only in annealing history: as-deposited, 300, 400, 600 and 800°C. The differences among the PDFs are the result of annealing-induced change to the atomic structure. The letters represent sections of PDF where the most significant changes are observed: (a), (b) and (d) change in intensity, (c) new peaks appearing, (e) and (f) shift in peak positions. Section (d) is magnified in the inset to highlight the systematic change as a function of annealing temperature.

atomic level processes that cause the changes seen in the PDFs, it is essential to develop atomic models that are sensitive enough to capture the observed changes in PDFs. A common method of choice is to follow a regression algorithm that fits atomic coordinates with the measured PDFs, e.g. simulated annealing [15] or reverse Monte Carlo (RMC) [16] etc. However, the changes caused by annealing are subtle even for the two extreme ends of annealing (viz as-deposited and 800°C annealed) and hence one faces an interesting problem and requirement: how to reliably generate two slightly different structural solutions of an otherwise identical disordered system? Conventional modeling techniques often fail to resolve subtle changes in atomic structure with high fidelity, especially in the IRO, which makes it difficult to give definitive statements about the changes in structure.

We follow an integrated modeling approach that seeks to maximally constrain the solution space by using all *a priori* information. In this work, the set of *a priori* information consisted of density-functional-theory-based atomic models, a classical two-body force field, density and composition measurements on thin films, and the X-ray GIPDF measurements. These data are used to guide an RMC-based high-throughput modeling routine. In order to have the correct atomic ratio and supercell size in our models, we measured the composition and density in our samples using Rutherford Back-scattering Spectrometry (RBS) and used the results to constrain the composition and density of the models (see [10]). The measured PDFs show some structure up to a distance of $\sim$ 15 Å and

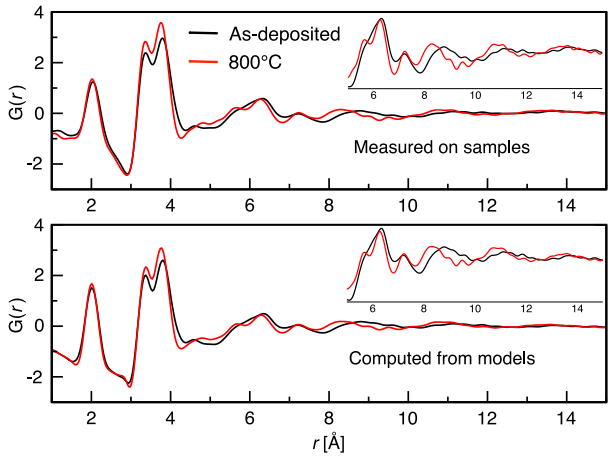

FIG. 2. **Measured and computed PDFs:** The measured PDFs from two samples (top) are compared with PDFs computed from atomic models (bottom). The PDFs are grouped to highlight that the atomic models are able to closely track the annealing-induced changes in PDFs. Computed PDFs in the bottom plot are averages of over 1000 independent models. The 5 Å to 15 Å section of PDFs in each plot are shown in higher resolution in insets. See [10] for plot involving all four samples.

accordingly the supercell size of the model is chosen to be able to compute G(r) up to 15 Å. Using the composition and density from the RBS measurements, we generated starting configurations of zirconia-doped tantala by employing melt-quench molecular dynamics (MD) simulations where we used two-body empirical potentials from [18, 19]. These configurations are then modified using RMC until the computed PDF matches with the GIPDF data. However, it is well known that a traditional RMC produces non-physical solutions, even in elemental systems [20]. We used *ab initio* molecular dynamics (AIMD) to generate smaller models (190 atoms) of the same system, and the distribution of bond-lengths present in the AIMD models was used as a constraint to RMC. This was done by requiring that the metal-oxygen bond distances lie in the range predicted by the partial PDFs of AIMD models (see [10]). Furthermore, following the "FEAR" method [21], RMC moves were interspersed with energy minimization moves iteratively until the desired agreement with experiments was obtained. The entire modeling algorithm was repeated to get 1000 independent atomic models corresponding to each of the four samples i.e. as-deposited, 300°C annealed, 600°C annealed and 800°C annealed. All the properties reported hereafter are computed by averaging over 1000 models. Figure 2 shows the ability of the models to capture the changes on measured PDF up to 15 Å; to the best of our knowledge, it is the first demonstration that atomic models can capture changes in IRO up to 15 Å with such a high accuracy. It should be emphasized here that the models reported in this work are chemically realistic i.e. they contain no non-physical metal-metal chemical bonds. The models, by construction, have density and composition that are representative of the IBS coatings. In the following, we show that the deductions made from the models agree with experiments and the structural features computed from the models show a systematic trend with annealing temperature. A plot showing the fit of the structure factor S(q) and G(r) along with additional information on the modeling method is given in the supplementary material [10].

In the following, we present a discussion of the structure of a-Ta_2O_5:ZrO_2 based on the models we obtained. As in many glass-forming materials like silica, the structure of a-Ta_2O_5:ZrO_2 can be described as a 3-dimensional network of metal (M)-centred coordination polyhedra that have oxygen (O) atoms at their corners. The M-O correlation gives rise to the first peak. The polyhedra are predominantly distorted octahedra (∼80% for Ta, ∼60% for Zr, [10]). It has been shown that the first peak of G(r) for pure a-Ta_2O_5 closely resembles to the corresponding peak of crystalline Ta_2O_5 [13]. We find that the coordination of Ta by O (n_{TaO}) is 6.13 whereas n_{ZrO} is 6.14; both values are for un-annealed sample. The measured value of n_{TaO} using ^{17}O NMR studies on IBS deposited pure a-Ta_2O_5 is 6.1(3) [22, 23]. The M-O bond distance peaks at 2.0(2) Å and it is comprised of a Ta-O sub-peak at 1.98 Å and and a Zr-O sub-peak at 2.06 Å. The slight difference in Ta-O and Zr-O bond distances is also consistent with *ab initio* models; it is likely that this difference is helpful in frustrating the crystallization of tantala [24]. As a result of annealing, coordination of M by O (n_{MO}) shows a small but consistent trend to smaller values, and a corresponding change, although small, in the M-O bond distance towards a lower value is observed in the total G(r) (see figure 10 in [10]). The structure within the first coordination sphere of tantala has been extensively characterized [7, 13, 25, 26].

The polyhedra link with each other through O-atoms at each corner. Each O-atom is at least 2-coordinated with metal atoms. The ratio of 2-coordinated to 3-coordinated O-atoms is ∼ 1:2, which is notably different from pure tantala where the value measured using NMR is 2:3 [22, 23]. The difference comes from O-atoms bonding preferentially 3-fold with Zr; the mean O-coordination by M is 2.7 (see inset of figure 3(e)). The correlation between two metal atoms connected by at least one O-atom gives rise to the second peak in total G(r). It is interesting to note the bifurcation in the M-M peak into two sub-peaks at 3.35 Å and 3.75 Å since similar measurements in pure tantala show the first sub-peak at 3.35 Å at much reduced intensity [13, 25]. Its much more pronounced presence in the mixed phase is an effect of doping by zirconia and has structural implications in that the first and second peaks originate from correlations of edge-sharing (ES) and corner-sharing (CS) polyhedra respectively (figure 3(b)). For the as-deposited

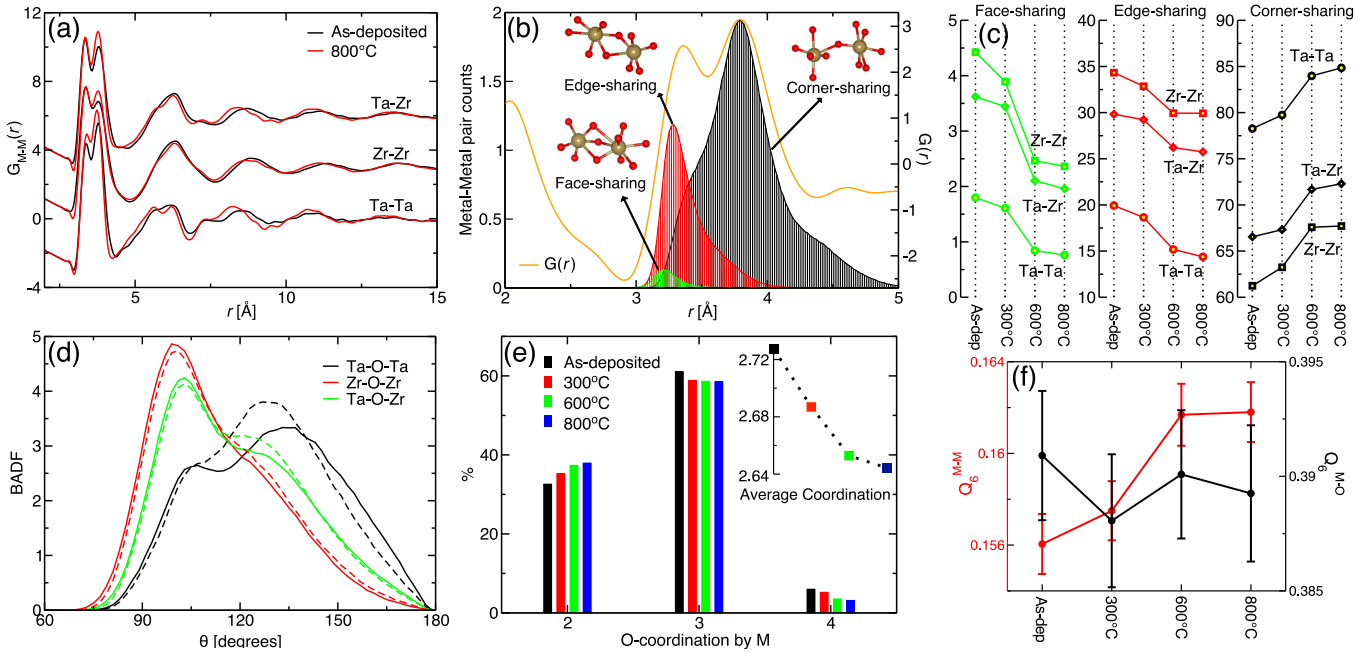

FIG. 3. **Structural fingerprints of annealing:** Plots of major structural trends in the models. All results are averages over 1000 models. When it applies, an M-O bond cutoff distance of 2.9 Å is used. This distance is the minimum directly after the first peak in total G(r). (a) Partial PDFs for M-M pairs are plotted. (b) Origin of the double hump in G(r) as correlations between corner and edge shared M-M pairs. The orange line represents total G(r). The shaded regions represent the distribution of M-M pair distances separated on the basis of the number of O-atoms they share. A shared O-atom is the one that lies within the bond cutoff distance from both M-atoms. (c) The evolution percentages of corner-, edge-, and face- shared M-M pairs with annealing. (d) BADF from the as deposited (the dashed lines) and 800°C annealed models (e) Distribution of O-coordination by M for samples with different annealing history. Inset shows the averaged coordination vs annealing temperature. (f) BOO parameters (Q_6) [17] as a function of annealing temperature. The black and red dots show the Q_6 for M-O and M-M correlations. The error bars are standard deviations. The dots are connected to guide the eyes.

sample, the ratio of CS to ES correlations is 3.93 for Ta-Ta, 2.23 for Ta-Zr, and 1.78 for Zr-Zr. There is also a small concentration of face-sharing (FS) polyhedra where the polyhedra share 3 O-atoms between them.

The effect of annealing is much more pronounced beyond the first M-O peak and all the way to 15 Å. Many of the changes observed in the total G(r) can be explained by considering the partial M-M correlation (figure 3(a)), where changes are observed from ∼3 Å all the way up to 15 Å. First of all, the peaks become narrower and sharper suggesting that annealing increases the order in M-M correlation lengths. Since the bifurcated M-M peak represents the correlations between the polyhedra, the annealing induced change in the peak signifies that annealing alters the mode by which polyhedra connect with each other. An analysis presented in figure 3(c) shows that the concentration of CS polyhedra increases as a result of annealing whereas it decreases for ES and FS polyhedra. The effect of the overall decrease of density of ES and FS polyhedra is that the average O-coordination by M decreases as a function of annealing temperature (see figure 3(e)). A decrease in O-coordination upon annealing was also observed for pure tantala using ^{17}O NMR studies in [23]. An analysis of the M-O-M bond angle distribution function (BADF) shows that BADF, in general, narrows and shows a more defined peak upon annealing 3(d). However, there is a more characteristic change in BADF that is worth noting: each M-O-M BADF curve shows a double peak and the peak around 120° to 130° increases with annealing. Further analysis shows that the characteristic two-peak BADF arises from the presence of ES and CS polyhedra; the increase in M-O-M BADF around 120° to 130° is caused by increase in the ratio of CS to ES polyhedra (see figure 9 in [10]).

We use the bond orientational order (BOO) parameter Q_6 [17] to quantify the degree of disorder present in the models. The BOO parameter corresponding to M-O bonds, denoted by $Q_6^{\text{M-O}}$ in figure 3(f), shows that there is no significant effect of annealing in the M-O coordination sphere. We also probed the degree of order among the polyhedral units by computing $Q_6^{\text{M-M}}$ among the metal atoms and the values suggest an increase in BOO with annealing, a trend clearly seen in the measured G(r). To the extent $Q_6^{\text{M-M}}$ is a measure of IRO among the polyhedral units, it is noteworthy to observe an inverse correlation of $Q_6^{\text{M-M}}$ with measured values of mechanical loss at room temperature (see figure 1 in [10]). Future modeling experiments are planned to directly compute the

mechanical loss on these structures [27], which will help elucidate the role of IRO in mechanical loss.

The experimental observations, atomistic models, and resulting atomic structure analysis suggest the following consequences of annealing:

1. There is evidence of subtle change in first coordination sphere around M-atoms in that M-coordination by O decreases upon annealing and M-O bond distance trends to a smaller value.

2. The major effect of annealing is found to be the change in the way the polyhedral units organize themselves in the film. The ratio of edge-sharing to corner-sharing M-M polyhedra decreases upon annealing and, as a corollary, the average O-coordination by M decreases.

3. There is a hint of an increased order in M-M correlation as indicated by narrowing and sharpening of M-M peaks in partial PDFs and increase in the computed values of $Q_6^{\text{M-M}}$.

It is observed experimentally that as a result of annealing tantala-based coatings the mechanical loss at room temperature decreases [8, 10, 28, 29]. The dissipation mechanism for mechanical loss is often conceptualized as two-level systems (TLSs) which are asymmetric double-wells separated by an energy barrier. TLSs arise from subtle rearrangements of clusters of atoms [27, 30]. The observed trends in mechanical loss with annealing suggests that ES-polyhedra are more likely associated with TLSs that contribute to room temperature mechanical loss, whereas the CS-polyhedra that form lower barrier height TLSs contribute to low temperature mechanical loss. This conjecture is bolstered by the observation that silica, which has nearly 100% CS polyhedra has low loss in room temperature and high loss at low temperature [31]. If this conjecture is correct, then in order to reduce mechanical loss at room temperature one would aim to have a material that produces less ES-polyhedra and more CS-polyhedra. Conversely, a material with less CS-polyhedra and more ES-polyhedra would likely reduce mechanical loss at low temperature. As doping with zirconia helps suppress the crystallization but increases the ratio of ES-polyhedra, the doping percentage of zirconia is a key variable to optimize in order to reduce mechanical loss at room temperature. In particular, a lower concentration of zirconia that is just enough to suppress the crystallization would be desirable. Indeed, in a study by Tewg et al. [24], lower zirconia doping concentrations in tantala were observed to suppress crystallization, with a highest crystallization temperature measured from a sample with $\text{Zr}/(\text{Zr}+\text{Ta}) \simeq 0.33$. Investigations are currently underway for thin films with varying levels of zirconia doping concentrations.

In conclusion, we have presented a detailed study on the effect of annealing on zirconia-doped tantala amorphous thin films using a combination of experimental data and modeling routines. Upon annealing, there are subtle changes observed in the SRO, but the most significant change is the increase in IRO. The GIPDF measurement method and the modeling scheme employed in this work represent a significant step forward for the detailed study of the atomic structure of amorphous thin films, providing a powerful tool capable of accurately capturing subtle changes in the atomic structure up to 15 Å. Important to the particular usage case of reducing thermal noise in interferometric gravitational-wave detectors, caused by mechanical loss in the mirror coatings, our analysis and interpretation suggests that, compared to the $\text{Zr}/(\text{Zr}+\text{Ta}) \simeq 0.48$ measured here, lowering the zirconia doping concentration merits further study and is the subject of ongoing research.

We acknowledge the support of the LSC Center for Coatings Research, jointly funded by the National Science Foundation (NSF) and the Gordon and Betty Moore Foundation. In particular, the authors are grateful for support through NSF awards PHY-1707866 and PHY-1708175. CL, FS and RS are grateful for support from the NSERC, CFI, and FQRNT. IWM is supported by a Royal Society Research Fellowship. We are also grateful to Ric Shimshock at MLD Technologies for useful discussions and for providing thin film samples. We acknowledge support from Bill Baloukas and Ludvik Martinu of cole Polythechnique de Montral for access to ellipsometry and stylus profilometry instruments. Use of the Stanford Synchrotron Radiation Lightsource, SLAC National Accelerator Laboratory, is supported by the U.S. Department of Energy, Office of Science, Office of Basic Energy Sciences under Contract No. DE-AC02-76SF00515.

* prasai@stanford.edu
† rbassiri@stanford.edu

[1] N. Hinkley, J. Sherman, N. Phillips, M. Schioppo, N. Lemke, K. Beloy, M. Pizzocaro, C. W. Oates, and A. Ludlow, Science **341**, 1215 (2013).
[2] G. M. Harry, H. Armandula, E. Black, D. Crooks, G. Cagnoli, J. Hough, P. Murray, S. Reid, S. Rowan, P. Sneddon, *et al.*, Applied optics **45**, 1569 (2006).
[3] S. Hild, Classical and Quantum Gravity **29**, 124006 (2012).
[4] S. R. Elliott, Longman Group, Longman House, Burnt Mill, Harlow, Essex CM 20 2 JE, England, 1983. (1983).
[5] S. R. Elliott, Nature **354**, 445 (1991).
[6] L. Červinka, Journal of Non-Crystalline Solids **106**, 291 (1988).
[7] R. Bassiri, K. Borisenko, D. Cockayne, J. Hough, I. MacLaren, and S. Rowan, Applied Physics Letters **98**, 031904 (2011).
[8] I. W. Martin, R. Bassiri, R. Nawrodt, M. Fejer, A. Gretarsson, E. Gustafson, G. Harry, J. Hough, I. MacLaren, S. Penn, *et al.*, Classical and Quantum Gravity **27**,

225020 (2010).
[9] M. J. Hart, R. Bassiri, K. B. Borisenko, M. Véron, E. F. Rauch, I. W. Martin, S. Rowan, M. M. Fejer, and I. MacLaren, Journal of Non-Crystalline Solids **438**, 10 (2016).
[10] See supplementary information for additional information on the simulation method and further numerical results.
[11] P. Fuoss and A. Fischer-Colbrie, Physical Review B **38**, 1875 (1988).
[12] A. Fischer-Colbrie, A. Bienenstock, P. Fuoss, and M. A. Marcus, Physical Review B **38**, 12388 (1988).
[13] B. Shyam, K. H. Stone, R. Bassiri, M. M. Fejer, M. F. Toney, and A. Mehta, Scientific Reports **6**, 32170 (2016).
[14] X. Qiu, J. W. Thompson, and S. J. Billinge, Journal of Applied Crystallography **37**, 678 (2004).
[15] S. Kirkpatrick, C. D. Gelatt, and M. P. Vecchi, Science **220**, 671 (1983).
[16] D. Keen and R. McGreevy, Nature **344**, 423 (1990).
[17] P. J. Steinhardt, D. R. Nelson, and M. Ronchetti, Physical Review B **28**, 784 (1983).
[18] J. Trinastic, R. Hamdan, Y. Wu, L. Zhang, and H.-P. Cheng, The Journal of Chemical Physics **139**, 154506 (2013).
[19] J. Yu, R. Devanathan, and W. J. Weber, Journal of Materials Chemistry **19**, 3923 (2009).
[20] D. Drabold, The European Physical Journal B **68**, 1 (2009).
[21] A. Pandey, P. Biswas, and D. A. Drabold, Scientific Reports **6**, 33731 (2016).
[22] N. Kim and J. F. Stebbins, Chemistry of Materials **23**, 3460 (2011).
[23] N. Kim and J. F. Stebbins, Journal of Non-Crystalline Solids **378**, 158 (2013).
[24] J.-Y. Tewg, Y. Kuo, and J. Lu, Electrochemical and Solid-state Letters **8**, G27 (2005).
[25] O. L. Alderman, C. Benmore, J. Neuefeind, E. Coillet, A. Mermet, V. Martinez, A. Tamalonis, and R. Weber, Physical Review Materials **2**, 043602 (2018).
[26] R. Bassiri, F. Liou, M. R. Abernathy, A. C. Lin, N. Kim, A. Mehta, B. Shyam, R. L. Byer, E. K. Gustafson, M. Hart, *et al.*, APL Materials **3**, 036103 (2015).
[27] J. P. Trinastic, R. Hamdan, C. Billman, and H.-P. Cheng, Physical Review B **93**, 014105 (2016).
[28] G. Vajente, R. Birney, A. Ananyeva, S. Angelova, R. Asselin, B. Baloukas, R. Bassiri, G. Billingsley, M. Fejer, D. Gibson, *et al.*, Classical and Quantum Gravity **35**, 075001 (2018).
[29] G. M. Harry, M. R. Abernathy, A. E. Becerra-Toledo, H. Armandula, E. Black, K. Dooley, M. Eichenfield, C. Nwabugwu, A. Villar, D. Crooks, *et al.*, Classical and Quantum Gravity **24**, 405 (2006).
[30] P. Fedders and D. Drabold, Physical Review B **53**, 3841 (1996).
[31] K. Topp and D. G. Cahill, Zeitschrift für Physik B Condensed Matter **101**, 235 (1996).

Supplementary information: High precision detection of change in intermediate range order of amorphous zirconia-doped tantala thin films due to annealing

Kiran Prasai,[1,*] Jun Jiang,[2] Alec Mishkin,[2] Svetoslava Angelova,[3] Ross Birney,[3] David A Drabold,[4] Mariana Fazio,[5] Eric Gustafson,[6] Gregory Harry,[7] Sarah Hoback,[7] Carl Lévesque,[8] Ian MacLaren,[9] Iain W Martin,[9] Carmen S Menoni,[5] Steven Penn,[10] Stuart Reid,[3] Raymond Robie,[9] François Schiettekatte,[8] Rosalie Shink,[8] Badri Shyam,[11] Gabriele Vajente,[6] Hai-Ping Cheng,[2] Martin M Fejer,[1] Apurva Mehta,[12] and Riccardo Bassiri[1,†]

[1]*E. L. Ginzton Laboratory, Stanford University, Stanford, California 94305, USA*
[2]*Department of Physics and Quantum Theory Project, University of Florida, Gainesville, Florida 32611, USA*
[3]*SUPA, Department of Biomedical Engineering, University of Strathclyde, Glasgow G1 1QE, United Kingdom*
[4]*Department of Physics and Astronomy, Ohio University, Athens, Ohio 45701, USA*
[5]*Department of Electrical and Computer Engineering, Colorado State University, Fort Collins, Colorado 80523, USA*
[6]*LIGO Laboratory, California Institute of Technology, Pasadena, California 91125, USA*
[7]*Department of Physics, American University, Washington, DC 20016, USA*
[8]*Department of Physics, Université de Montréal, Québec H3T 1J4, Canada*
[9]*SUPA, School of Physics and Astronomy, University of Glasgow, Glasgow G12 8QQ, UK*
[10]*Department of Physics, Hobart and William Smith Colleges, Geneva, New York 14456, USA*
[11]*University of Dayton Research Institute, Dayton, Ohio 45469, USA*
[12]*SLAC National Accelerator Laboratory, Menlo Park, California 94025, USA*

(Dated: January 18, 2019)

S1. Motivations for studying zirconia-doped tantala

The work presented in this letter is a part of research directed at identifying low Brownian thermal noise optical coatings for the test masses of the LIGO gravitational wave detectors. The current generation of the LIGO detectors use highly reflective dielectric coatings for its core-optics, which consist of alternating layers of amorphous silica and titania-doped-tantala. At the most sensitive frequency range (~ 40 - 200 Hz), these coatings give rise to a limit in the detector sensitivity due to Brownian thermal noise. The dominant source of Brownian thermal noise arises from the mechanical loss in the high-refractive index titania-doped-tantala layers, with a mechanical loss of $\sim 2 \times 10^{-4}$. For the Advanced LIGO + upgrade, planned to start commissioning in 2021, a coating with at least a factor of two improvement in mechanical loss is required (mechanical loss $\leq 1 \times 10^{-4}$).

The current coatings for LIGO optics are deposited using ion-beam sputtering (IBS). One of the ways of reducing the thermal noise at room temperature of thin film coatings is post-deposition annealing. It has been shown that post-deposition annealing of tantala up to the temperatures of 600°C, prior to the onset of crystallization, reduces the room temperature mechanical loss of the coatings [1]. Doping amorphous tantala with zirconia at a ratio of Zr/(Ta+Zr) = 0.33 can suppress crystallization, allowing the films to remain amorphous after annealing up to 800°C [2].

The mechanical loss was measured at room temperature as a function of post-deposition annealing temperature from similar coatings used for GIPDF analysis of zirconia-doped tantala (Zr/(Ta+Zr) $\simeq$ 0.48) coatings. The results shown in figure 1 indicate that, as with pure tantala, the mechanical loss of zirconia-doped tantala decreases with increasing post-deposition annealing temperature. As indicated in figure 1, the annealing time is extended for temperatures at 600°C and above, but appears to have little effect at 600°C compared to the annealing temperature. Interestingly, the 800°C annealed sample has a loss of 1.8×10^{-4}, which is slightly below the currently employed titania-doped tantala coatings, and demonstrates that zirconia-doped tantala is a promising coating material system that warrants further study as a potential Advanced LIGO + coating.

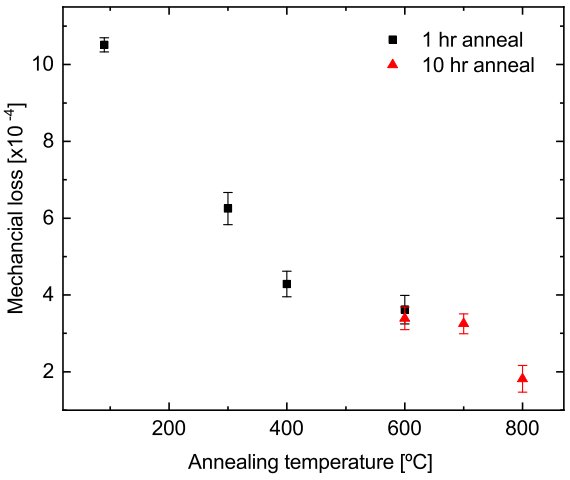

FIG. 1. Mechanical loss at room temperature for zirconia doped tantala as a function of annealing temperature. For details of the measurement process see Refs. [3].

S2. Density and composition of samples

We measured the composition, density and thickness of two of the four samples used in GIPDF measurements. Those two samples are as-deposited and 800°C annealed. The composition was determined using Rutherford Backscattering Spectrometry (RBS) [4] analysis where the samples were exposed to a beam of α particles at an energy of 2.9 MeV at normal incidence and the back-scattered particles were detected at 170°. Atomic concentrations were determined by fitting a simulated spectra to the measured spectra. The best fit was obtained at the concentrations given in table I.

TABLE I. **Composition measurements using RBS**

	Atomic Concentration (%)	
Element	**As deposited**	**800°C annealed**
Ta	16.00±0.15	15.50±0.15
Zr	14.8±0.3	14.8±0.3
O	66.4±1.5	67.0±1.5
Ar	2.8±0.4	2.7±0.4

Areal densities of the samples were also obtained from RBS to be 4370±90 × 10^{15} atoms/cm^2 for both as-deposited and 800°C annealed samples. The thicknesses of the samples were measured, using combinations of stylus profilometry and ellipsometry [5, 6] measurements, to be 589±4 nm and 587±10 nm for as-deposited and 800°C annealed samples respectively. Thickness measurements, combined with areal density and composition measurements from RBS, enabled us to calculate mass densities of the samples to be 6.53±0.15 gm/cm^3 for as-deposited sample and 6.53±0.18 gm/cm^3 for 800°C sample.

Following these measurements, we used a stoichiometric ratio of 15:67.5:15 for Ta, O and Zr respectively for all our models. We have not included Ar atoms in our models because the x-ray scattering signature of ∼2.5% Ar is low (see figure 2) and because our separate DFT based calculations (not shown here) indicate that Ar atoms have a negligible effect on the structure of the material itself. We used a density of 6.53 gm/cm^3 for our models, but we did take into account a mass of 2.5% Ar to obtain the effective box-size for our models. After considering the mass of Ar atoms, the effective density in our models is 6.41 gm/cm^3. The size of our models is chosen to enable computation of G(r) up to 15 Å which is the distance up to which measured GIPDF shows some degree of IRO. With all of these considerations in place, our final models have 400 Ta, 1800 O and 400 Zr in a cubic box of dimension 32.92 Å.

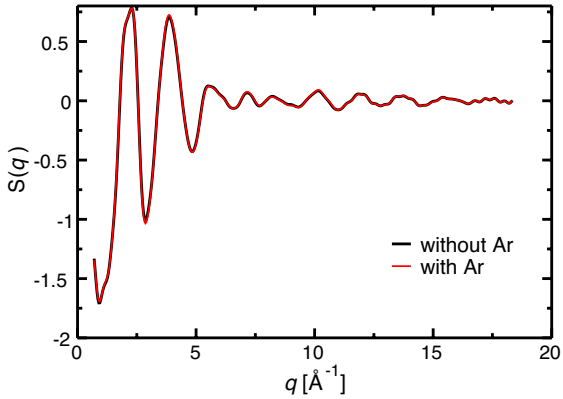

FIG. 2. The x-ray structure factors, S(q), computed from the models. The red curve is from a model which has Ta, O, Zr and Ar atoms in the ratio 15:67.5:15:2.5. The black curve represents when the Ar atoms were removed from the model.

S3. Integrated modeling approach

The modeling scheme that is used to obtain the atomic models presented in this work is further illustrated here. The flowchart in figure 3(a) shows the sequence of steps followed to obtain the final models. The modeling algorithm starts by considering 1000 independent systems where each system has 2600 randomly positioned atoms in a cubic supercell; a threshold distance of 1.9 Å between is maintained between the atoms even for random positions. The atomic ratio and density are chosen as discussed in section S2 and are kept fixed. These models are taken through a conventional melt-quench MD modeling cycle (as discussed in section S5). The final configurations from MD serve as the starting configuration for the RMC models. RMC moves are set to fit to the measured S(q) and are constrained by enforcing a distance window of 1.5 Å to 2.9 Å for Ta-O bond distance and of 1.5 Å to 3.2 Å for Zr-O bond distance. M-M lower cutoff of 2.9 Å and O-O lower cutoff of 2.0 Å were also used to constrain the RMC moves. These distances correspond to the lower and upper cutoff of the corresponding partial PDFs of AIMD-based models (see discussion in section S4 and figure 5). RMC moves and energy minimization moves are iterated back and forth until a convergence in chi-squared (degree of misfit) and a convergence in the total energy are reached. This iterative approach was first proposed as force enhanced atomic relaxation (FEAR) in [7, 8]. The final models from this process are considered as representative of the samples on which the GIPDF measurements were made. To get a better statistical accuracy, we repeat the process for 1000 independent models and take an average for all quantities reported in the paper. The plot of the fitted structure factor (S(q)) and the corresponding plot in real space is presented in figure 3(b) and (c).

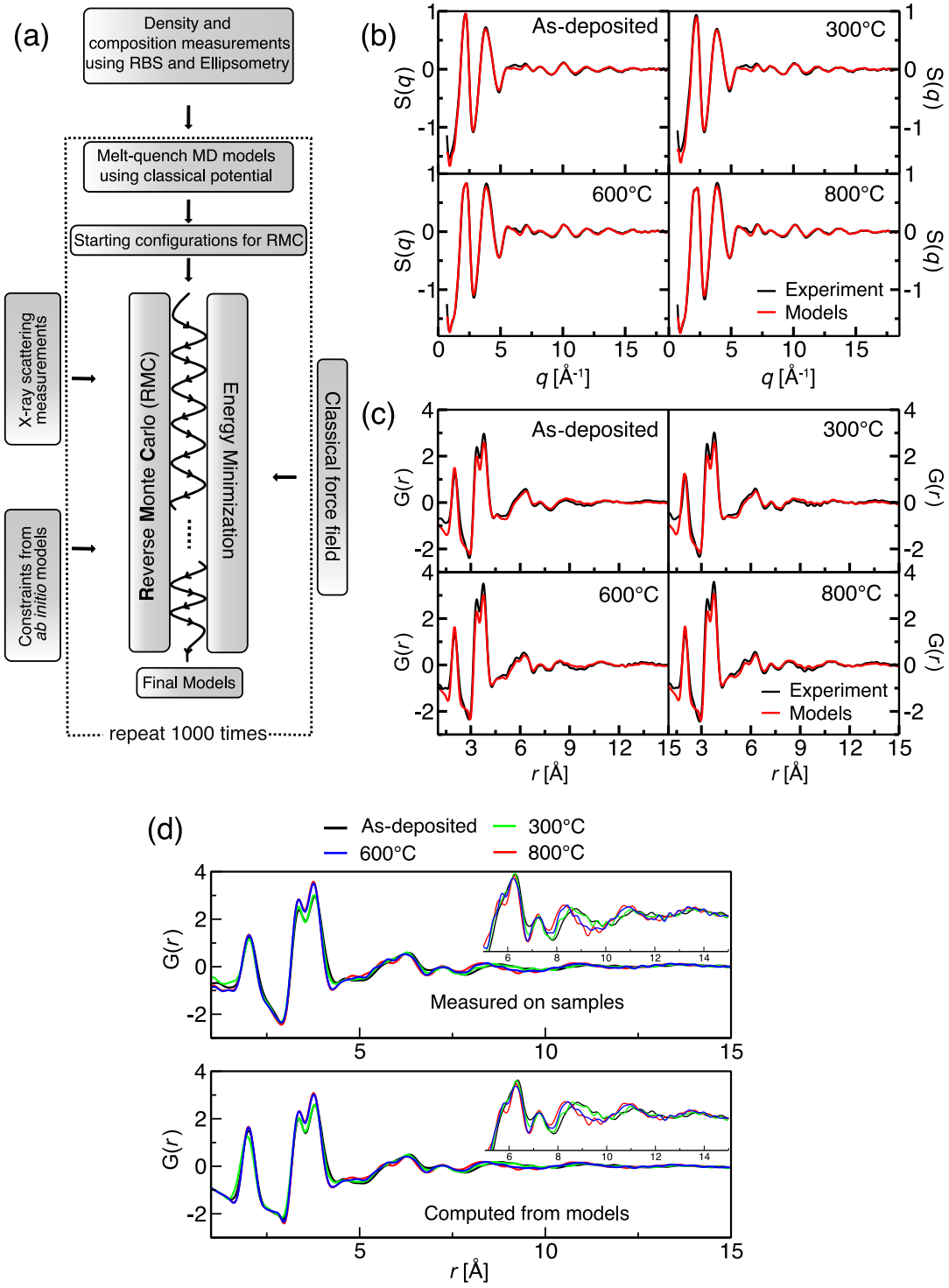

FIG. 3. **More on the modeling approach and results** (a) The integrated modeling approach: Illustration of how *ab initio* MD, classical MD, RMC based on measure GIPDF data and density and composition measurements of thin films are combined together to obtain models that are realistic and sensitive to annealing induced changes in the structure. (b) Goodness of fit: The structure factor, S(q), measured on samples is compared the corresponding fitted models. The computed S(q) are averages over 1000 models. (c) The computed G(r) on models are compared with G(r) obtained from GIPDF measurements. The computed G(r) are averages over 1000 models. (d) The ability of the computed models to track the changes in IRO seen in the measured G(r) at different annealing temperature. This figure is the complete version of figure 2 in main paper.

S4. Melt-quench models using *ab initio* molecular dynamics (AIMD)

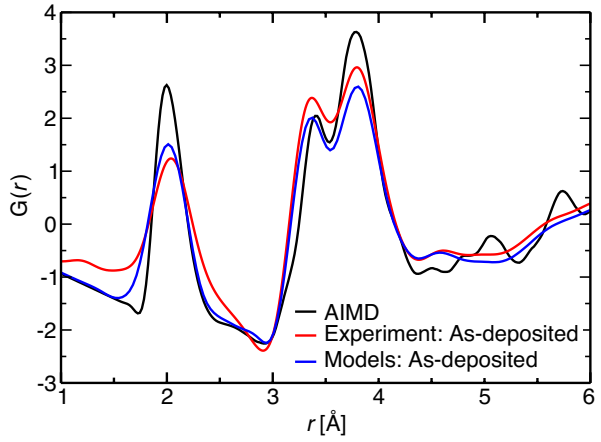

FIG. 4. The total G(r) of AIMD models is compared with measured G(r) and the computed G(r) from RMC based models.

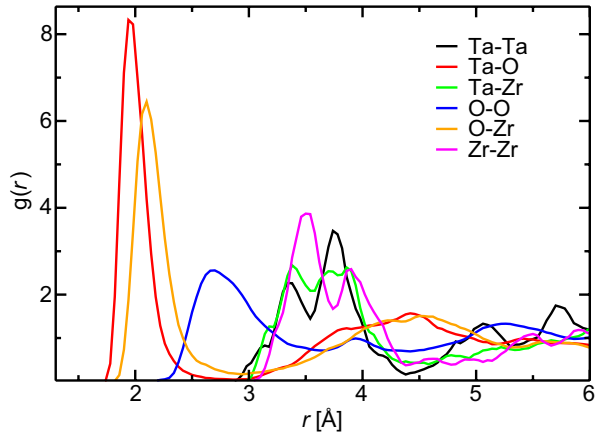

FIG. 5. The partial G(r) computed on AIMD models. Note that the definition of G(r) used in this plot is different the definition of G(r) used in the paper. In this case, $g_{\alpha\beta} = \frac{V}{4\pi r^2 N_\alpha}\frac{dn_{\alpha\beta}}{dr}$, where V is volume of supercell, N_α is number of species α, and $dn_{\alpha\beta}$ is the number of β atoms at distance r to $r+dr$ from α atom. This definition of G(r) is useful to help infer the cutoffs for atomic correlations. Additionally, the area under the partial G(r) give the corresponding coordinations as a function of r.

We performed *ab initio* molecular dynamics (AIMD) to obtain smaller atomic models of zirconia-doped tantala. The purpose of this exercise was to provide geometrical constraints to bond distances during RMC modeling and also to enable basic sanity checks on our main models. 30 Ta atoms, 30 Zr atoms and 135 O atoms are taken in a cubic supercell of dimensions 13.78 Å and periodic boundary conditions were applied. This is equivalent to a bulk mass density of 6.55 gm/cm^3. In order to create the starting configuration for AIMD, the system is first taken through a melt-quench molecular dynamics cycle employing an empirical force field [9, 10] over a total time period of 1.15 ns. LAMMPS simulation software was used [11]. The starting configuration obtained is then taken through an AIMD melt-quench cycle using Vienna *ab initio* software package (VASP) [12, 13]. PBE functionals were used [14, 15] and valence electrons were treated using plane waves of upto 400 eV. The system was equilibrated at 4000 K, then at 2500 K, then quenched to 300 K, and then again equilibrated at 300 K. Total simulation time for the melt-quench dynamics was 104.6 ps, wherein time steps of 2 fs were used throughout the simulation. The computed G(r) from AIMD models is compared with measured G(r) and computed G(r) from RMC-based models in figure 4.

S5. Melt-quench models using classical molecular dynamics (CMD)

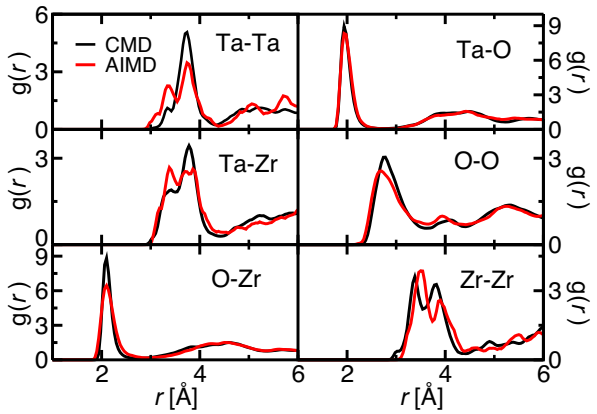

FIG. 6. Partial PDF from MD models: The partial PDFs obtained from the melt-quench MD modeling described in section S4 and S5 are plotted here for comparison. CMD denotes the models using classical molecular dynamics as described in section S5. AIMD denotes the *ab initio* molecular dynamics described in section S4. The partial PDFs from CMD are averages of 1000 snapshots of the model over 100 ps of MD at 300 K; each model contains 975 atoms. The partial PDFs from AIMD are averages of 7844 snapshots of the model over 15.7 ps of MD at 300 K; each model contains 195 atoms.

We use a unified classical two-body potential from references [9, 10] to perform the energy minimization component of our modeling (see figure 3). To investigate the ability of the potential to predict basic structural features, we carried out melt-quench molecular dynamics simulation in the framework of the classical potential. We used the LAMMPS simulation program [11] as follows: A random collection of 975 atoms (of type Ta, O and Zr atoms in the ratio discussed in section S2) in a supercell of size determined by the density is taken. Constant pressure (NPT) MD simulations were carried out at various starting densities (viz 6.0, 6.3, 6.55, 6.7, 7.0 and

7.5 gm/cm^3). For all simulations, the system was taken to a high temperature of 6000 K, equilibrated at that temperature, then cooled down to 300 K and equilibrated again at 300 K. The total number of steps was more than 1.3 $\times 10^6$ which corresponds to more than 1.3 ns of simulated time. The structures were finally relaxed to its minimum energy configurations using conjugate gradient algorithm. The final density of all the models converged to $\sim$6.8 gm/cm^3. In figure 6, we compare the partial PDFs of these models with the AIMD generated models (described in section S4). We find that the CMD predicts the basic features of the partial PDF correctly, although the M-M correlations are not predicted very well. The energy minimization with respect to the referenced force-field is a useful constraint, however one needs to be careful about how it interferes with the overall models. Note that the melt-quench MD used to generate the starting configurations for RMC modeling follows the same routine as described in this section, except that those models contain 2600 atoms and constant volume (NVT) ensemble is used for MD.

S6. Further plots on coordinations and bond angle distributions

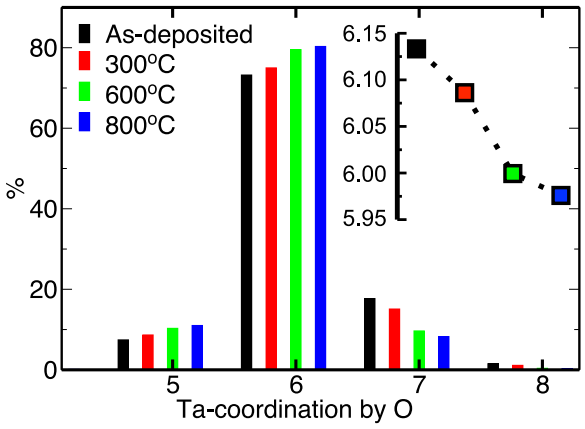

FIG. 7. The distribution of Ta-coordination by O atoms in our models. The bond cutoff is taken to be 2.90 Å which is the first minimum of total G(r). The coordination values are averages over 1000 models. The inset shows the average coordination number for the four samples.

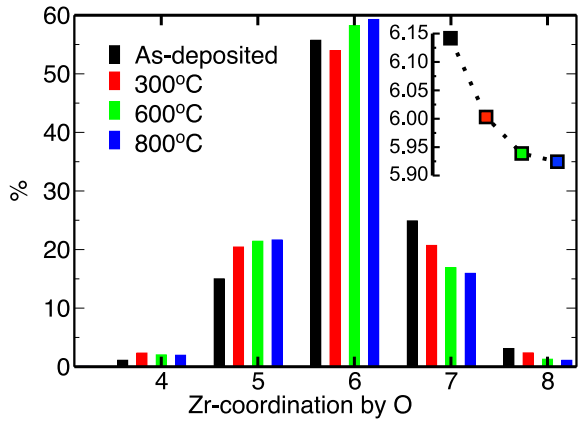

FIG. 8. The distribution of Zr-coordination by O atoms in our models. The bond cutoff is taken to be 2.90 Å which is the first minimum of total G(r). The coordination values are averages over 1000 models. The inset shows the average coordination number for the four samples.

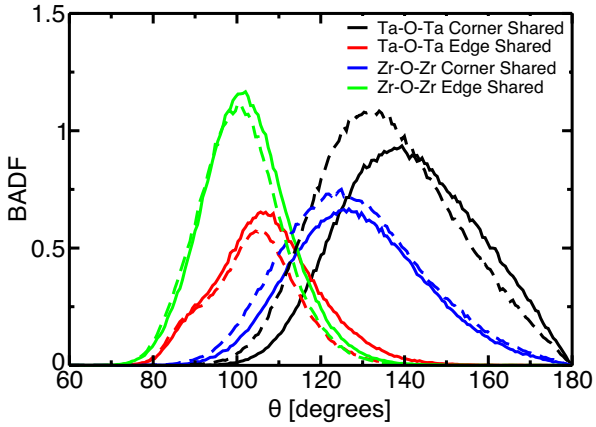

FIG. 9. BADF resolved into edge-sharing and corner-sharing polyhedra for Ta-O-Ta and Zr-O-Zr. Solid line represents as deposited sample and dashed line represents 800°C annealed sample.

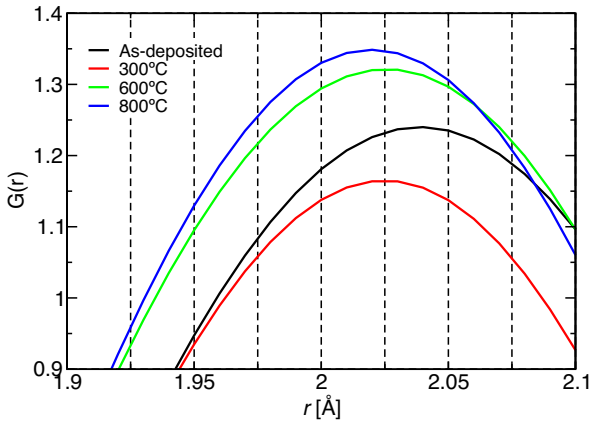

FIG. 10. The first peak in G(r) in high resolution. The positions of first peak correspond to M-O bond lengths.

* prasai@stanford.edu
† rbassiri@stanford.edu

[1] G. Vajente, R. Birney, A. Ananyeva, S. Angelova, R. Asselin, B. Baloukas, R. Bassiri, G. Billingsley, M. Fejer, D. Gibson, *et al.*, Classical and Quantum Gravity **35**, 075001 (2018).
[2] J.-Y. Tewg, Y. Kuo, and J. Lu, Electrochemical and Solid-state Letters **8**, G27 (2005).
[3] G. Vajente, A. Ananyeva, G. Billingsley, E. Gustafson, A. Heptonstall, E. Sanchez, and C. Torrie, Review of Scientific Instruments **88**, 073901 (2017).
[4] W.-K. Chu, *Backscattering spectrometry* (Elsevier, 2012).
[5] A. Piegari and E. Masetti, Thin solid films **124**, 249 (1985).
[6] H. Fujiwara, *Spectroscopic ellipsometry: principles and applications* (John Wiley & Sons, 2007).
[7] A. Pandey, P. Biswas, and D. A. Drabold, Scientific Reports **6**, 33731 (2016).
[8] A. Pandey, P. Biswas, and D. Drabold, Physical Review B **92**, 155205 (2015).
[9] J. Trinastic, R. Hamdan, Y. Wu, L. Zhang, and H.-P. Cheng, The Journal of Chemical Physics **139**, 154506 (2013).
[10] J. Yu, R. Devanathan, and W. J. Weber, Journal of Materials Chemistry **19**, 3923 (2009).
[11] S. Plimpton, Journal of Computational Physics **117**, 1 (1995).
[12] G. Kresse and J. Hafner, Physical Review B **47**, 558 (1993).
[13] G. Kresse and J. Furthmüller, Physical Review B **54**, 11169 (1996).
[14] P. E. Blöchl, Physical Review B **50**, 17953 (1994).
[15] J. P. Perdew, K. Burke, and M. Ernzerhof, Physical Review Letters **77**, 3865 (1996).